# Concurrent OH imager and sodium temperature/wind lidar observation of localized ripples over northern Colorado

Tao Li, C. Y. She, Bifford P. Williams, and Tao Yuan
Department of Physics, Colorado State University, Fort Collins, Colorado, USA

Richard L. Collins
Geophysical Institute and Department of Electrical and Computer Engineering, University of Alaska Fairbanks, Fairbanks, Alaska, USA

Lois M. Kieffaber and Alan W. Peterson
Department of Physics, Whitworth College, Spokane, Washington, USA

Received 9 April 2004; revised 23 February 2005; accepted 1 April 2005; published 12 July 2005.

[1] On 3 and 5 September 2002 the OH all-sky imager at Platteville, Colorado (40.2°N, 104.7°W), observed small-scale, wavelike patterns (known as ripples), with horizontal wavelengths of ~9 km and ~7 km and lifetimes of ~9 min and ~15 min, respectively. The Colorado State University sodium lidar at nearby Fort Collins, Colorado (40.6°N, 105°W), also made concurrent observations of temperature and zonal and meridional winds, which allowed us to determine the nature of the ripples observed. Our observations suggest that the 3 September ripple was induced by a convective instability located at 87.5 km and the 5 September ripple was induced by a dynamic instability at 88.5 km. The ripples clearly advected as packets with the background wind. Lidar measurements also allowed us to relate the directions of wind shear to the phase front alignments of both the ripples and the nearby short-period atmospheric gravity waves. These spatial relationships provided a meaningful comparison with previously observed ripples as well as with current theoretical models. Using the 16-hour continuous lidar data set for each case, we deduced that long-period waves created an unusually large temperature perturbation at the ripple times on 3 September and an unusually large wind shear perturbation on 5 September. These perturbations prepared the background atmosphere to be near the verge of local instability, but, as revealed again by lidar observation, it was the superposition of smaller-scale perturbations at the time of the ripples that helped to actually reach the conditions required for instability and generation of the ripples.

**Citation:** Li, T., C. Y. She, B. P. Williams, T. Yuan, R. L. Collins, L. M. Kieffaber, and A. W. Peterson (2005), Concurrent OH imager and sodium temperature/wind lidar observation of localized ripples over northern Colorado, *J. Geophys. Res.*, *110*, D13110, doi:10.1029/2004JD004885.

## 1. Introduction

[2] Studies of atmospheric gravity waves (AGWs) have been prompted by the need to understand the contribution of these waves to both the variability [*Hines*, 1960] and general circulation [*Houghton*, 1978] of the middle atmosphere. Breaking AGWs have been recognized to contribute to the general circulation through both the eddy diffusion created as the waves cascade to turbulence and the wave drag due to their momentum flux divergence [*Holton*, 1982]. Dynamic (or shear or Kelvin-Helmholtz) instabilities and convective (or Rayleigh-Taylor) instabilities provide the primary mechanisms for gravity wave breaking and dissipation in the middle atmosphere [*Fritts and Rastogi*, 1985]. The physical mechanism by which the AGWs break determines the magnitude of both the diffusion and the wave drag and hence the extent of influence of these waves on the general circulation. One of the major challenges has been the ability to make measurements of the wave-breaking events, instability signatures, and associated background atmosphere with sufficient resolution (<1 km,<300 s) and scope (e.g., temperature and winds, horizontal and vertical structure) to unambiguously determine their physical characteristics. The study of a class of small-scale, wavelike, localized patterns in airglow images, known as ripples, is important, because they are thought to be instability features generated in situ, and they are easily distinguishable from propagating AGWs [*Taylor et al.*, 1995, 1997; *Nakamura et al.*, 1999]. These ripples are then signatures of local instability in airglow images, and they may be related to, or even be, a step in a wave breaking process covering a larger local area. Since the 1980s, there has been steady progress in the observational techniques employed to yield


0148-0227/05/2004JD004885

such measurements, and in three-dimensional (3-D) simulations on instability dynamics and the associated transition to turbulence. A recent extensive review by *Fritts and Alexander* [2003] highlighted many of recent significant advances. In the same review, though not mentioning the term ripples, the authors summarized numerical studies on the role of convective and dynamic instabilities and their generation of convective billows and Kelvin-Helmholtz (KH) billows, in the transition from 2-D laminar flow to 3-D turbulence, accompanying the wave-breaking processes.

[3] *Peterson and Kieffaber* [1973] showed that airglow images could yield the horizontal structure of AGWs as they propagated through the airglow layer. Later observations revealed the presence of ripples in the images [*Peterson*, 1979; *Taylor and Hapgood*, 1990; *Swenson and Mende*, 1994, *Taylor et al.*, 1995, 1997; *Nakamura et al.*, 1999]. These structures were smaller in spatial scale (5–15 km in wavelength) and shorter in duration (<45 min) than the signatures of the propagating AGWs (often referred to as bands). They were limited in spatial extent (3 to 15 phase fronts) and were interpreted as the signatures of instability in the airglow layer. Early studies suspected that the ripple structures were the signatures of dynamic instabilities [*Taylor and Hapgood*, 1990] as 2-D analyses had indicated that the wave amplitude threshold for dynamic instability of an AGW was lower than for that convective instability [*Fritts and Rastogi*, 1985]. The combination of airglow imagers with wind and temperature profilers allowed researchers to investigate the instability hypothesis associated with the ripples directly. During the Collaborative Observations Regarding the Nightglow (CORN) campaign researchers combined OH and $O_2$ airglow imagers, temperature lidar and MF wind measurements with a 3-D fluid dynamic model observations to study a ripple event. Their observations and analysis of this event indicated that the ripple in question was a signature of a convective instability that arose because of the superposition of long-period and short-scale waves [*Hecht et al.*, 1997; *Fritts et al.*, 1997]. The authors concluded that while dynamic instability may be important in the early stages, the convective instability grows more rapidly and dominates the wave breaking process [*Andreassen et al.*, 1994; *Fritts et al.*, 1994; *Isler et al.*, 1994]. Alternatively, *Hecht et al.* [2001] combined MF radar wind measurements and OH and $O_2$ airglow imagers to study a ripple event and found that the observations were consistent with a dynamic instability.

[4] The exact interpretation of ripples (i.e., due to either convective or dynamic instability) and the alignment of their phase fronts can be complex and at times may appear to be ambiguous. In a recent article, *Hecht* [2004] provided a comprehensive review on the airglow studies of ripples observed, and provided a clear distinction between ripples (orientation and characterization), AGWs, and the local atmospheric conditions. The phase fronts of a ripple due to dynamic instability, i.e., KH billows, are perpendicular to the wind shear vector. For a wind speed shear, the phase fronts of the associated AGWs would be parallel to the KH ripple phase fronts. For a wind directional (or rotational) shear, they can be at an angle to each other. The ripple structure resulting from convective instability was much less well known [*Hecht* ]. *Fritts et al.* [1997] showed via simulation that in a convective instability the ripple phase fronts were aligned perpendicular to the phase of the "unstable or breaking" AGW. However, once formed, the "convective billows" became detached and rotated by the local wind shear [*Fritts et al.*, 1996]. Indeed, *Yamada et al.* [2001] recently reported a small-scale wavelike feature, thought to be ripples due to convective instability, which were aligned parallel to the breaking wave fronts and concluded that the convective billows is rotated to align with the background wind shear. Table 1 summarizes past ripple observations along with one recent case observed over Hawaii [*Li et al.*, 2005] and two cases reported here, and the accompanying diagnostics. Depending on the characteristics of a ripple, its phase front may be either parallel or perpendicular to the propagation vector of the associated short-period gravity wave, k, or to the direction of local wind shear vector, ws. This will be discussed in more detail below and it is denoted for each case observed in the column 6 of Table 1.

[5] Another observable parameter associated with ripples is the ratio of the spacing between ripple phase fronts (wavelength) to the depth of the instability region. Studies of winds have shown that this ratio is approximately 8 in the case of dynamic instability [*Lloyd et al.*, 1973; *Larsen*, 2000], while 3-D numerical simulations by *Fritts et al.* [1994, 1997] have shown that this ratio should be approximately 2 in the case of convective instability. A clear indication that ripples are signature of instability (convective or dynamic) is the fact that once formed, ripples will advect with the background wind.

[6] Recent high-resolution lidar observation of temperature and horizontal wind has enabled studies of atmospheric instability. *Zhao et al.* [2003] analyzed 32 nights of such lidar measurements throughout the year and determined that convective and dynamic instabilities in the mesopause region occurred with similar frequencies. With 7 nights and 70 hours observation between 26 January and 14 February, *Sherman et al.* [2003] deduced a higher probability of dynamic instability. Perhaps coincidentally, among the eight ripples listed in Table 1 with sufficient diagnostics, four were thought to be associated with convective and four with dynamic instabilities. Zhao et al. also found that the atmospheric tides had a considerable influence on the probability of occurrence of instabilities: While the tides themselves usually are not sufficient to induce instability, the superposition of the tides with short-period AGWs can be sufficient to render the local atmosphere unstable. A case study of high-resolution sodium wind-temperature lidar measurements in 4 nights combined with a model and modeled mean profiles was recently made by *Liu et al.* [2004], concluding that the observed convective and dynamic instabilities were induced by the combination of AGWs and tides.

[7] In this paper, we present sodium temperature/wind lidar and OH airglow imager measurements of the instability features observed on two nights (2–3 September 2002 and 4–5 September 2002, or 3 September and 5 September, UT) over northern Colorado. The lidar wind and temperature measurements provide quantitative measurements of the atmospheric conditions, characterizing both the tidal activity and local atmospheric instabilities. We analyze the nature of the ripples in terms of the structure of the

**Table 1.** Selected Ripple Studies With Concurrent Lidar Radar Observations[a]

| Authors | Instability | Ripple λ | GW λ | Lifetime τ | Ripple Phase F | Diagnostic |
|---|---|---|---|---|---|---|
| *Peterson* [1979] | ... | 10–15 km | ... | <30 min | ... | no |
| *Taylor and Hapgood* [1990] | dynamic | 12 km | 24 km | ... | parallel to k | no |
| *Hecht et al.* [1997] | convective | <10 km | 30–50 km | <20 min | parallel to k | lidar T |
| *Nakamura et al.* [1999] | ()[b] | <15 km | 18–60 km | >10 min | ()[b] | no |
| *Hecht et al.* [2000] | convective | <10 km | 27 km | <10 min | parallel to k | lidar T |
| *Yamada et al.* [2001] | convective | <10 km | 27 km | ~40 min | perpendicular (parallel) to k (ws) | radar W |
| *Hecht et al.* [2001] | dynamic | 7–9 km | 48 km | ~30 min | perpendicular to k;ws | radar W |
| This work (2–3 Sept.) | convective | 9 km, | 43 km | ~9 km | parallel to k;ws | lidar T,W |
| This work (4–5 Sept.) | dynamic | 7 km | 38 km | ~15 min | parallel (perpendicular) to k(ws) | lidar T,W |
| *Li et al.* [2005] | dynamic | 12 km | 44 km | ~20 min | parallel (perpendicular) to k(ws) | lidar T,W |

[a]GW, gravity wave; k, propagation direction of small-scale gravity wave; ws, direction of wind shear; T, temperature; W, wind.
[b]Many case studies without exploring types of instability.

background atmosphere, thus reporting one of the few such studies accompanied by concurrent observation of both temperature and horizontal wind with a high-resolution lidar. Our characterization of the local mesopause region was done by two lidar beams separated by ~70 km, operated for a duration much longer than the lifetime of the ripples. In this case, there were 16 hours of continuous temperature and wind measurements on each day. In what follows, we first describe, in section 2, the capability and methodology of the OH image and the two-beam lidar used for this study. This is followed by the observations and characterization of the ripples in section 3. We discuss the ripple events observed on each night separately, and discuss the atmospheric stability during each ripple with data from lidar observations. Here, we also compare the nature of the ripples we observed to those of others and to the properties predicted by theory/simulation. In section 4, we present lidar measurements of the background atmosphere, examining the relative importance of tidal perturbations in relation to local instabilities that lead to the in situ generation of ripples. These are then followed by discussions, providing caveats and raising a number of questions, and conclusions in sections 5 and 6, respectively.

## 2. Instrumentation and Methodology

[8] The facility for ground-based optical observation in the Fort Collins/Platteville area was deployed in 2001 as a part of NASA/NSF TIMED/CEDAR collaboration (Thermosphere Ionosphere Mesosphere and Electrodynamics is a NASA satellite devoted to the study of atmosphere between 60 and 180 km, and Coupling Energetic Dynamics of Atmospheric Regions is a NSF ground-based observation program). The main instrumentation consists of an all-sky imager and a two-beam narrowband sodium lidar. The OH all-sky imager is located in Platteville, Colorado (40.2°N, 104.7°W), with a useful half field of view of 70°. The two-beam lidar is located at Fort Collins, Colorado (approximately 70 km NW of Platteville), with north and east beams that are separated by ~70 km, each having a beam diameter of ~100 m in the mesopause region. The lidar beams are well within the field of view

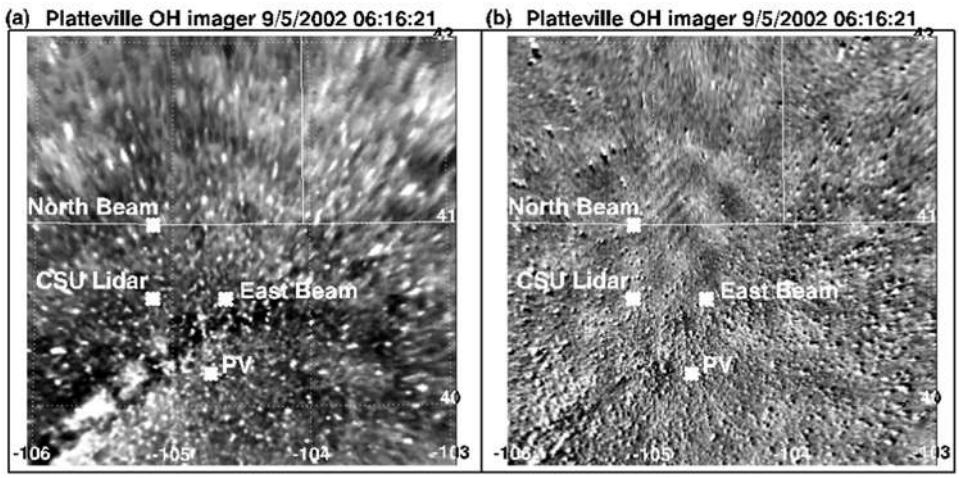


**Figure 1.** Example of ripples observed on (a) the flat field raw image on 0616:21 UT, 5 September 2002, as compared to (b) the flat field difference image made by subtracting successive images. The size of the image is 250 × 250 km. A ripple at the immediate northwest of the north beam can be seen clearly on the difference image. Though not as clear, the ripple can also be seen at the same location in the raw image.

of the all-sky imager. Their relative locations are marked within the OH images (Figure 1).

[9] The Platteville OH imager has been acquiring IR all-sky images of the OH airglow layer (~87 ± 4 km) in nighttime at a 2 min cadence since September 2001. The imager uses a Nikon f/2.8 fisheye lens to give 180 degrees field of view. It has a broadband OH filter (680–980 nm) with a cut-on feature at 680 nm. The CCD camera is an Apogee AP6 with a Kodak front-illuminated 1024 × 1024 CCD chip binned to 512 × 512 with a 120 s exposure time. The CCD chip sensitivity governs the low-wavelength cutoff before the filter does. The broadband OH filter also transmits $O_{2A}(0,1)$ emission [*Broadfoot and Kendall*, 1968], but since the result of a recent campaign revealed a less than 10% contamination by $O_2$ airglow [*Shiokawa et al.*, 1999], the adverse interference from it on wave patterns should be minimal. Furthermore, for this paper, the altitude where instability signature (ripple) occurs is mainly determined by the lidar observations of instability layers, the exact OH peak height is not as important.

[10] To process the raw image data, we first rotated and shifted the images to place the North Star at the proper altitude and azimuth. Then, in order to look at short-period waves, we subtracted successive 2 min images to form difference images. This subtracted out the nonvarying background light and much of the star background. The differencing acts effectively as a low-pass filter, with maximum response at 4 min periods, falling off as the period increases. The difference images were scaled to ±40 count limits, compared to a typical value of 1000 counts in the raw image. This gives us a range of ±4% with waves visible down to less than 1% perturbation. If a raw image is desired, we process individual raw image of 2 min resolution with a 3 × 3 pixel median filter to minimize stars. Then, we make a flat field of each image by dividing a 40-min running time mean image. Further analysis was done by visually reviewing the flat field individual raw and/or difference images. For this study, we made flat fields of the images and zoomed in to a 250 × 250 km view centered on the lidar. Shown in Figure 1 are the flat field normalized raw and the difference OH images at 0616:21 UT, 5 September, both showing a ripple structure near the north lidar beam. Though the ripple can be seen more clearly in the difference image (Figure 1b), it is clearly visible in the raw image (Figure 1a) as well.

[11] The Colorado State University (CSU) narrowband Na lidar began its upgrade from a one-beam to a two-beam system in 1999. The upgraded two-beam system was designed for the simultaneous measurement of mesopause region Na density, temperature, and zonal and meridional wind profiles with both daytime and nighttime observational capabilities. Two Celestron 14 (35 cm in diameter) telescopes are used to receive the lidar signals. The size of this lidar is quite modest, and corresponds to a power-aperture product of 0.06 $Wm^2$ for each beam. The lidar signals consist of photon profiles of Na fluorescence from east and north beams, each pointing 30° from zenith. The signal is integrated in every 2 min and saved at 150 m bin to produce a raw photon count profile from each beam. The measurement precisions for temperature and wind with 2 km spatial resolution and 1-hour integration were estimated under nighttime fair ondition to be, respectively, 0.5 K and 1.5 m/s at the Na peak (92 km), and 5 K and 15 m/s at the edges (81 and 107 km) of the sodium layer. Faraday filters are inserted into the receiver to permit observations in sunlight [*Chen et al.*, 1996]. These Faraday filters reduce the detected background in the photon count profiles by an estimated factor of 6000–8000. However, the received signal is also reduced by a factor of 4–5, making the measurement uncertainty, when the Faraday filter is in use, larger by at least a factor of ~2.5, depending on sky irradiance. Though still by no means a turnkey instrument, the CSU two-beam narrowband Na lidar has been fully functional since May 2002, producing expected data quality and stability for long-period observation, weather permitting.

[12] For this study, we smoothed the raw photon count profiles to different resolutions depending on specific investigations. For the assessment of tidal perturbations, we used data acquired from ~16-hour continuous observation each day with 1-hour integration and smoothed the profiles to a vertical resolution of 2 km during nighttime and 4 km under sunlit conditions. For nighttime data when ripples occurred, we used (15 min, 2 km) and (15 min, 1 km) smoothing for background wind shear determination and for atmospheric stability assessment, respectively. The corresponding measurement errors are plotted along with values in the altitude profiles.

## 3. Observations of Ripples and Their Characterization

[13] We visually inspected all the raw and difference OH images taken from our Platteville OH imager on a frame-by-frame basis, from which interesting cases worthy of investigation were selected. An unusual event, consisting of clear small-scale, wavelike patterns was first noted on the night of 4–5 September 2002. In the process of examining AGW activity, we not only noticed stronger wave activity on the night of 2–3 September, we also found another ripple passing the lidar beams at nearly the same time in the night. During the nine hours on the night of 4–5 September we observed two more patches of ripples within the imager field of view, relative to the lidar beams, one in the southeast between 0800 and 0830, and the other in the southwest between 1020 and 1100 UT. Unlike the ripples we report here, each patch consisted of a group of 2–3 ripples moving together, and the ripples wavelength was larger, ~15 km. Though we saw strong AGW activity (or band-like structures) throughout the nine hours on the night of 2–3 September, the reported ripple was the only one we observed that night.

[14] The concurrent lidar data measurement of temperature and wind profiles permits experimental determination of Brunt-Vaisala frequency squared, $N^2$, and the (gradient) Richardson number, Ri, defined as

$$N^2 = \frac{g}{T}\left(\frac{dT}{dz} - \frac{dT_{ada}}{dz}\right) \text{ and } \mathrm{Ri} = \frac{N^2}{S^2} \text{ with } S = \left[\left(\frac{du}{dz}\right)^2 + \left(\frac{dv}{dz}\right)^2\right]^{0.5} \quad (1)$$

where $-dT_{ada}/dz = \gamma_d = g/c_p$ is the dry adiabatic lapse rate with g and $c_p$ being, respectively, the gravitational

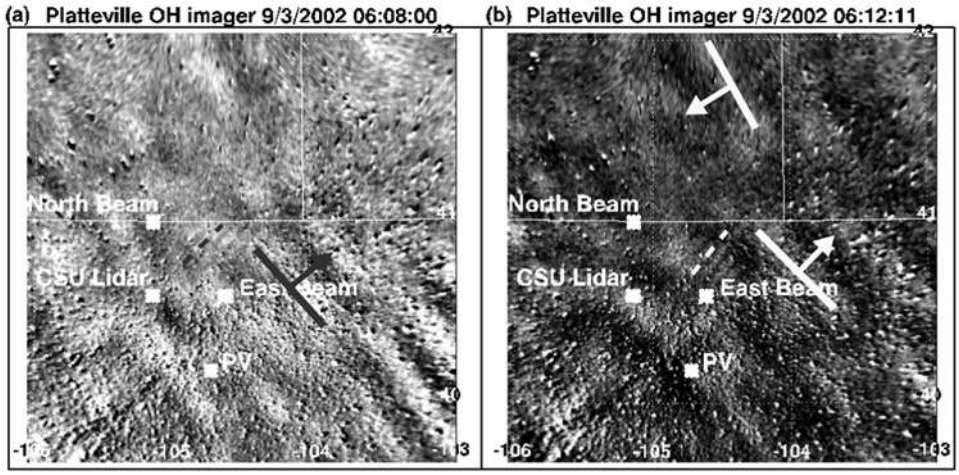


**Figure 2.** Two difference images at (a) 0608:00 UT and (b) 0612:11 UT taken on 3 September. A ripple with wavelength of ~9 km can be seen in both images, with one phase front each marked by a short dashed line to guide the eye. From the change in location of the ripple on successive images, 2 min apart, the motion of the ripple can be determined and tabulated in Table 2. Also shown are short-period gravity waves with phase front and propagation direction indicated by black or white line and arrow.

acceleration and per unit mass specific heat at constant pressure. Near 90 km altitude, the adiabatic lapse rate and g are 9.5 K/km and $9.5 \times 10^{-4}$ km $s^{-2}$, respectively. In equation (1), S, u, v and T are respectively, vertical shear of horizontal wind, zonal wind, meridional wind and temperature. The local atmosphere is said to be hydrostatically or convectively unstable if $N^2 < 0$. Simple theory suggests that $Ri > 0.25$ is a sufficient condition for dynamic stability [*Dutton*, 1986]. For clarity, we present the two ripple events separately.

### 3.1. Ripples Observed on the Night of 2–3 September

[15] Shown in Figure 2 are two selected difference OH images taken at 0608:00 UT (Figure 2a) and 0612:11 UT (Figure 2b), 3 September 2002. The 4 points marked in each image locate the center of the imager at Platteville (PV), CSU lidar facility at Fort Collins, and the east and north lidar beams in the mesopause region. These OH images show that the ripple passed by the east lidar beam. The wavelength (i.e., the crest-to-crest distance) of the ripple was measured to be ~9 km. The evolution of the ripple location in the sequence of images in 2-min intervals was recorded, allowing us to estimate the lifetime and to determine the motion of the ripple. For the ripple in question, they turned out to be, respectively, ~9 min (from 0605:55 to 0614:17 UT) and 40 m/s, 60° south of west. The ripple moved as a unit, or a packet, without distortion with intensity increasing and then faded away as it advected across the image with the background wind.

[16] To characterize the ripples and the associated instability, we examine in Figure 3 the temperature profiles of the east and north beams with adiabatic lapse rate marked (Figure 3a) and of zonal and meridional winds with selected wind gradients marked (Figure 3b). These profiles, centered at 0607:30 UT, 3 September, the time of the ripple, are smoothed to 15 min and 1 km resolutions. As indicated near 87 km, the measurement uncertainties are 3 K and 3.5 m/s for temperature and ntal wind respectively. At 87.5 km, the temperature slope of the east beam (solid line) matched the adiabatic lapse rate in Figure 3a, and the atmosphere was convectively unstable at this altitude, whereas the wind gradients at the same altitude in Figure 3b were relatively small. The corresponding profiles of Brunt-Vaisala frequency squared, $N^2$, and the gradient Richardson number, Ri, for the east beam are shown in Figures 3c and 3d, respectively. Taking the error bar into account, the $N^2$ is clearly seen to be negative at 87.5 km (Figure 3c), while the Richardson numbers at 87 km and 88 km in Figure 3d were greater than 0.25, suggesting that the observed ripple was associated with a convective instability. We have confirmed the nature of the instability by examining the potential temperature from the measured temperature profiles using standard procedures [e.g., *Williams et al.*, 2002; *Franke and Collins*, 2003]. The calculation of potential temperature is more robust than that of the Brunt-Vaisala frequency. The instability is observed during a period and in an altitude range where the potential temperature gradients approach zero and the contours of constant potential temperature are steep.

[17] The ripple was evidently present in the midst of a number of AGWs (or bands) in Figure 2 that were traveling in different directions as indicated by pairs of a black (or white) line and black (or white) arrow, indicating respectively the phase front and the propagation direction, k, of an AGW. Near the ripples, there was an AGW with phase fronts perpendicular to those of the ripples. The background hourly mean wind at 87.5 km as determined from lidar observation was 37 m/s at 50° south of west, revealing that the ripple was indeed moving with the background wind, as expected. Using the background wind, the intrinsic period of the AGW is then determined to be ~5.2 min. All these properties are tabulated in the second column of Table 2. From Figure 2, we note that the ripple phase fronts are perpendicular to the phase fronts of the nearby AGW (or parallel to its propagation direction, k) in agreement with the 3-D simulation [*Fritts et al.*, 1997; *Hecht*, 2004], as well

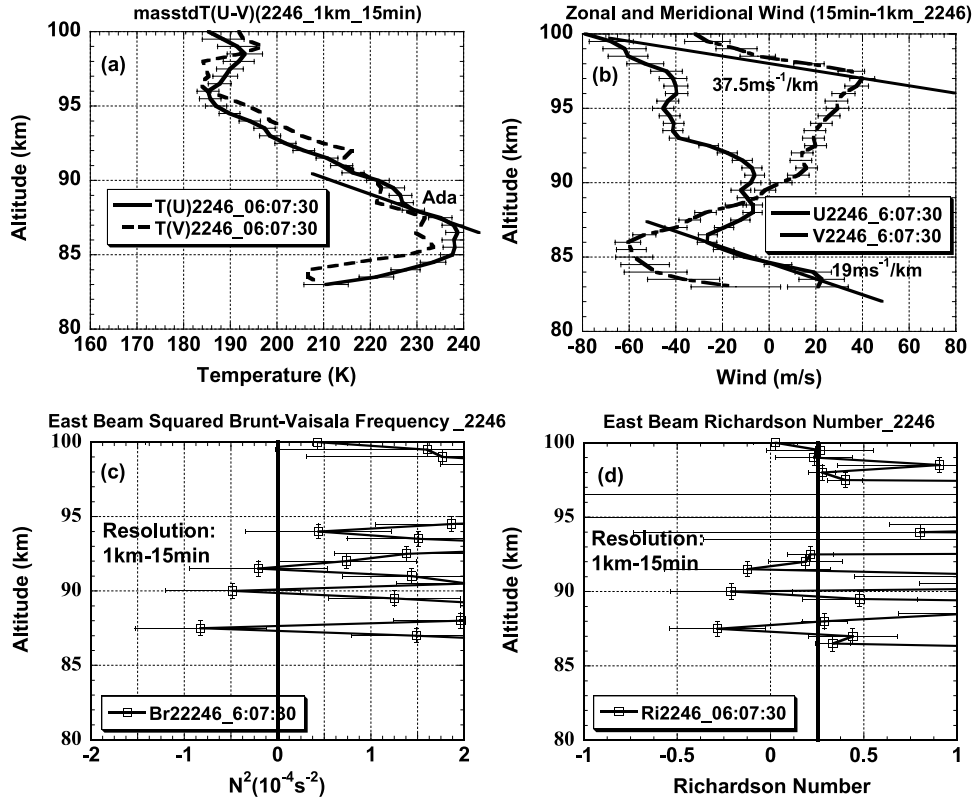


**Figure 3.** Fifteen-minute averaged profiles, centered on 0607:30 UT, 3 September, (a) of east beam (solid line) and north beam (dashed line) temperature profiles, (b) of zonal (solid line) and meridional (dashed line) winds, (c) of Brunt-Vaisala frequency squared, and (d) of Richardson number, based on east beam temperature.

as with convective billows observed by *Hecht et al.* [1997, 2000]. The ripple phase fronts we observed are also parallel to the wind shear direction at 87.5 km as shown in the hodogragh (Figure 4a). This is also consistent with the notion that once formed, the convective billows became detached and rotated by the local wind shear [*Fritts et al.*, 1996]. Since in our case the wind shear and the "initial" phase fronts of the convective billows are in the same

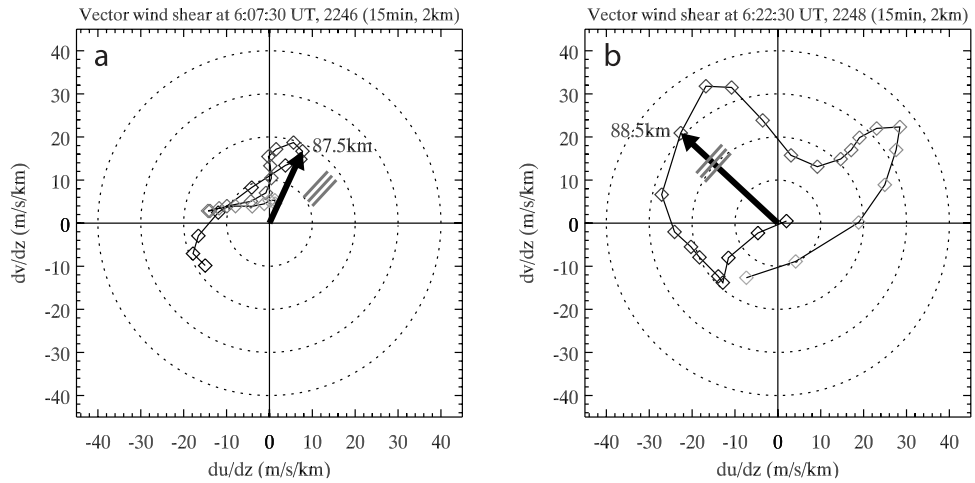


**Figure 4.** Polar plot of vertical shear of horizontal wind vectors at different altitudes, starting at 84 km (gray) and ending at 96 km (black), (a) centered at 0607:30 UT, 3 September, and (b) centered at 0622:30 UT, 5 September. The wind shear was computed from the zonal and meridional wind profiles centered with 15-min mean, 1 km resolution. The arrows give the wind shear vector at the height the ripples were thought to occur; they are approximately parallel and perpendicular to the ripple phase fronts in Figures 4a , respectively.

**Table 2.** Characteristics of Ripples and Associated AGW (Band)

| Parameters | Value (2–3 September) | Value (4–5 September) |
|---|---|---|
| Hourly mean horizontal wind speed and direction | 37 m/s at 87.5 ± 4 km, 50° south of west | 95 m/s at 88.5 ± 4 km, 56° south of west |
| GW phase speed | 100 m/s | 53 m/s |
| GW phase progression direction | 48° north of east | 42° north of east |
| GW horizontal wavelength | 43 km | 38 km |
| GW period (intrinsic) | 7.2 min (5.2 min) | 12 min (5.1 min) |
| $\omega - \omega_{int}$ | $-5.4 \times 10^{-3}$ rad/s | $-11.9 \times 10^{-3}$ rad/s |
| Ripple horizontal wavelength | 9 km | 7 km |
| Ripple packet moving speed | 40 m/s | 110 m/s |
| Ripple packet moving direction | 60° south of west | 50° south of west |
| Ripple alignment direction | 48° north of east | 42° north of east |
| Ripple duration | ~9 min | ~15 min |

direction, the ripples alignment needs not be altered, and its phase fronts remain perpendicular to the phase fronts of the associated unstable AGW.

[18] Contrary, when the background wind shear transverse to ripple phase fronts is appreciable, the local wind shear could alter the orientation of the ripples. In this case, the transition to isotropy and turbulence is slowed with a prolonged larger integrated effect [*Fritts et al.*, 1996]. Indeed, a very impressive case, displaying a 40-min evolution of turbulence dynamics with the observed ripples aligned parallel to the breaking AGW phase fronts (and wind shear), was reported by *Yamada et al.* [2001]; this is the only reported case we know that showed clear wave breaking over a larger area in the OH images. Unfortunately, in the study by *Yamada et al.* [2001], there existed a 12 min gap just before the first image that showed wave breaking, so we will never know whether or not an initial ripples with phase fronts aligned perpendicular to the phase fronts of associated (or breaking) AGW existed before the presumed reorientation by the wind shear takes place. Hopefully, with more airglow imagers now existing in sites with clustered diagnostics, we will soon see a case with the signatures of instability (convective or dynamic) followed by a full display of the various phases in the transition to turbulence in a wave breaking process [*Fritts and Alexander*, 2003]. Despite the fact that convective and/or KH billows were present at the initial stages of 3-D wave breaking simulations, it is of practical conveniences to distinguish between observations of a ripple, which is the signature of local atmospheric instability, from a wave-breaking events, where a large portion of the AGW breaks, since, to our knowledge, *Yamada et al.* [2001] reported, thus far, the only example of a wave-breaking event in the airglow image.

[19] We now turn to the ratio of ripple wavelength to the depth of instability region. According to simulations, this ratio should be about 2 for ripples induced by convective instability. *Hecht et al.* [1997, 2000] found this ratio to be between 3 and 4. Observational and numerical studies of instability are sensitive to the resolution of the studies [e.g., *Sica and Thorsley*, 1996; *Cutler et al.*, 2001], so care is needed in the measurement of the instability depth in terms of $N^2$ and Ri. With this caveat, we believe that the accuracies of both observation and simulation presently achieved to be sufficiently accurate to provide a meaningful comparison. In this connection, if we look at the instability layer near 87.5 km (see Figure 3c) the depth appeared to be about 1 km, yielding a ratio of roughly 9. We note, however, the existence of large error bars in $N^2$ and the spatial resolution of 1 km, so we cannot rule out a thicker instability layer (centered at 87.5 km) of up to 2 km. In addition, there existed 3 (unstable or near unstable) layers centered at 87.5, 90, and 91.5 km with $N^2 < 0$ at each of these altitudes, implicating a possible total depth of 4–

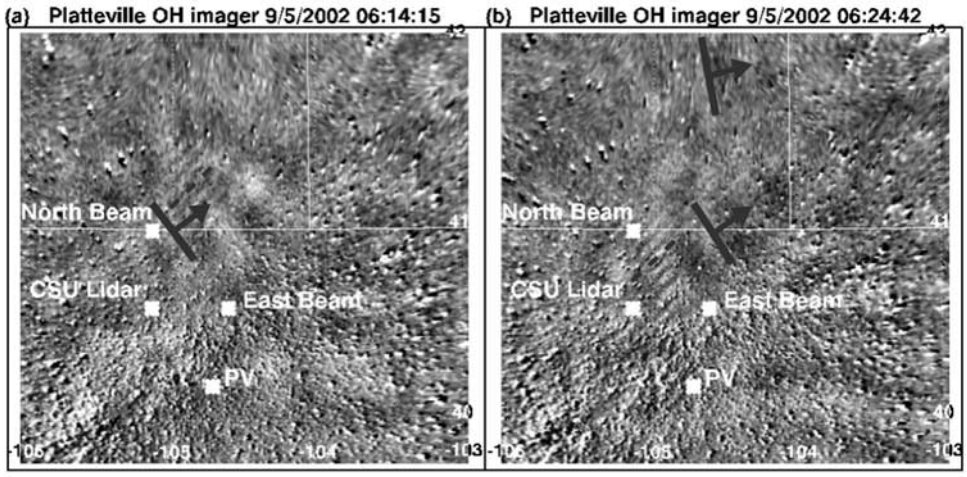


**Figure 5.** Same as Figure 2, except for images at (a) 0614:15 UT and (b) 0624:42 UT taken on 5 September, alo th the associated ripples and short-period propagating gravity waves that night.

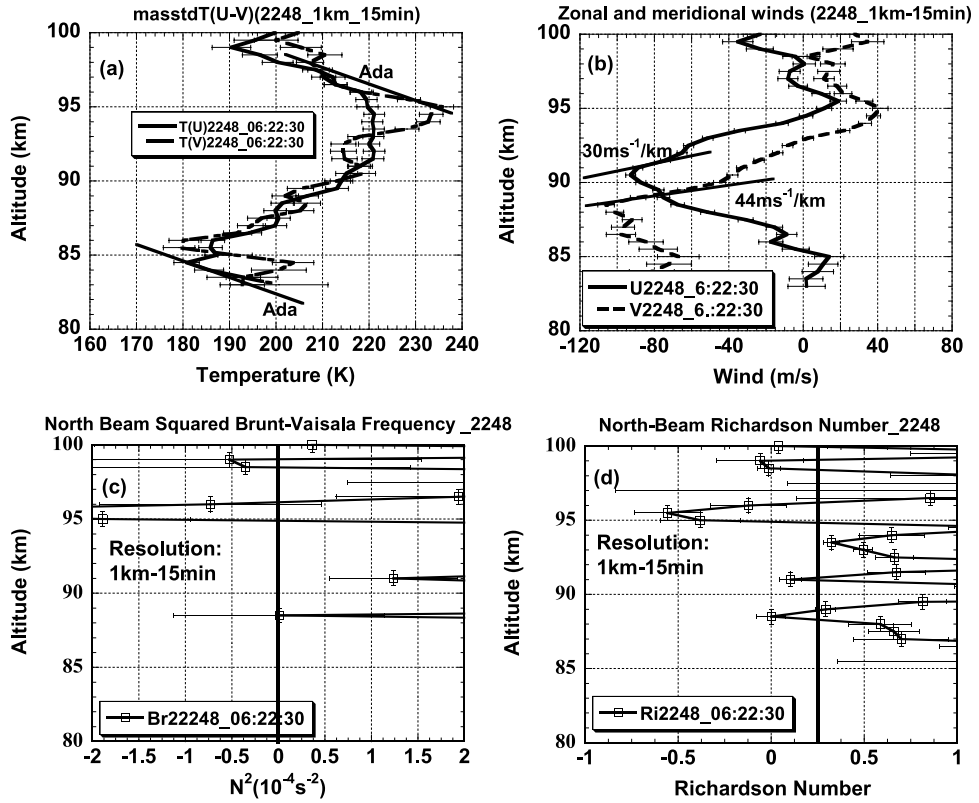


**Figure 6.** Same 15-min mean profiles as Figure 3, except centered on 0622:30 UT, 5 September. Also, Figures 6c and 6d are based on the north beam temperatures.

4.5 km. Since the observed ripple is presumably located in the OH layer, it likely signifies the existence of a single instability layer, giving an observed ratio of ripple spacing to instability depth between 4 and 5, consistent with the ratios reported by *Hecht* [2004]. To resolve this issue fully, better resolution and sharper definition of the instability depth will be needed for both observation and simulation. These await future studies.

### 3.2. Ripples Observed on the Night of 4–5 September

[20] Shown in Figure 5 are two selected difference OH images taken at 0614:15 UT (Figure 5a) and 0624:42 UT (Figure 5b), 5 September 2002. These OH images show that the ripple passed by the north lidar beam. Using the same methods described in section 3.1, we determined the wavelength, the lifetime, and the motion of the ripple to have been, respectively, ~7 km, ~15 min (from 0612:10 to 0626:47 UT) and 110 m/s, 50° south of west. Like before, the ripple moved as a unit without distortion with intensity increasing and then faded away as it transited with the background wind across the image.

[21] To characterize the ripples and the associated instability, we examine in Figure 6 the temperature profiles of the east and north beams with the adiabatic lapse rate marked (Figure 6a) and of zonal and meridional winds with selected wind gradients marked (Figure 6b). These profiles, centered at 0622:30 UT, 5 September, during the presence of the ripple structure, are smoothed to 15 min and 1 km resolutions. At 88.5 km, the temperature profiles of both beams in Figure 6a d that the atmosphere was convectively stable, while the meridional wind gradient at the same altitude in Figure 6b was about 44 m $s^{-1}$/km. The corresponding profiles of Brunt-Vaisala frequency squared, $N^2$, and the Richardson number, Ri, for the north beam where the ripples passes, are shown in Figures 6c and 6d, respectively. Taking the large error bar into account, the $N^2$ barely touches zero with hardly any layer depth (Figure 6c), while the error bars for Richardson numbers are small, with values at 0.25 for 88.5 km and near 0.25 for 88 km and 89 km (see Figure 6d), suggesting that the observed ripple was associated with a dynamic instability. We have confirmed the nature of the instability by examining the potential temperature. The instability is observed during a period and in an altitude range where the potential temperature gradients are positive and the contours of constant potential temperature remain horizontal.

[22] The ripple evidently was also in the midst of a number of AGWs (or bands) that were traveling in different directions as indicated in Figure 5. Near the ripple, there was an AGW with phase fronts perpendicular to those of the ripples. The background hourly mean wind at 88.5 km as determined from lidar observation was 95 m/s at 56° south of west, revealing that the ripple structure was generally moving with the background wind, as expected. The intrinsic period of the gravity wave was then determined to be ~5.1 min. All these properties are tabulated in the third column of Table 2. The ripple phase fronts we observed were, as expected, perpendicular to the wind shear direction at 88.5 km as shown in the hodograph (Figure 4b). This is in agreement with the KH billows observed by *Hecht et al.*

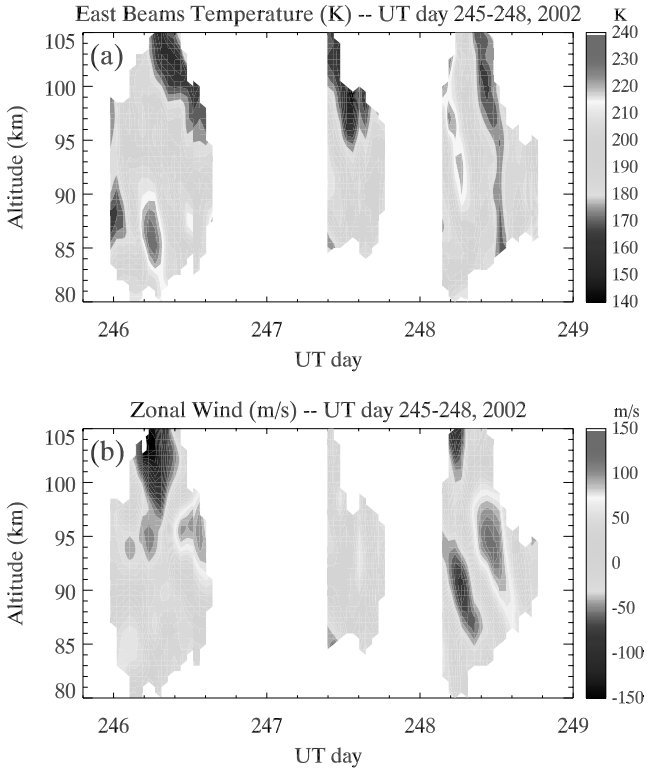


**Figure 7.** Altitude-time contour plots of (a) east beam temperatures and (b) zonal winds. The temperature data (Figure 7a) show a strong vertical temperature gradient between 85 and 90 km on 3 September. The zonal wind (Figure 7b) shows an unusually strong 12-hour perturbation between 85 and 95 km on 5 September. These are thought to be due to tidal period perturbations (see text). See color version of this figure at back of this issue.

[2001] and *Li et al.* [2005] as summarized in Table 1. From Figure 5, we note that the ripple phase fronts are perpendicular to the phase fronts of the associated AGW (or parallel to its propagation direction, k). Unlike that observed by *Hecht et al.* [2001], our case is in agreement with the KH billows observed by *Li et al.* [2005] (see the sixth column of Table 1). The difference likely lies in the fact that the local wind shear of *Hecht et al.* [2001] was a speed shear (similar to Figure 4a), while the wind shear in our case was a directional (or rotational) shear as can be seen clearly from the wind shear hodograph (Figure 4b). We now turn to the ratio of ripple wavelength to the depth of instability region. It is well known that this ratio for KH billows is roughly 8 [*Lloyd et al.*, 1973; *Larsen*, 2000]. Since with the usual caution, the depth of the layer with Ri < 0.25 at 88.5 km may be taken to have been 1 km, as shown in Figure 6d, the deduced ratio for our KH billows is 7–8, in agreement with theoretical and observational studies [*Lloyd et al.*, 1973; *Hecht et al.*, 2001; *Li et al.*, 2005].

## 4. Lidar Study of the Background Atmosphere

[23] With concurrent lidar measurement of temperature and horizontal wind, we were able to characterize the observed ripples in terms of local instabilities very well. The wind measurement it not only a confirmation of the fact that the ripples of either type (i.e., convective or dynamic instability), once formed, indeed move with the background wind, but also an assessment of the relative direction between the wind shear and the phase fronts of the ripples, thus making a connection between observation and theoretical expectation. The observations allow us to explore more questions. How did various atmospheric perturbations conspire to produce the temperature and wind gradients required to yield local instability? Did the long-period perturbations play an important role in the creation of the observed ripples? If so, can we identify these long-period waves? Was the presence of the short-period AGWs, often observed near the ripples, necessary to coherently enhance the temperature and wind gradients and lead to instability as suggested by simulation and model studies [*Hecht et al.*, 1997; *Fritts and Alexander*, 2003]?

[24] To provide some answers to these questions, we turn to the time evolution of the temperature and wind structures during the period in question for 3 and 5 September. Since the ripple observed around 0607:30 UT, 3 September (day 246), was associated with a convective instability, and that observed near 0622:30 UT, 5 September (day 248), was associated with a dynamic instability, we start out by showing the temperature and zonal wind contours during this period between 3 September and 5 September derived from hourly mean lidar profiles. At the OH heights, we see a strong temperature oscillation of 8–10-hour period on day 246 (Figure 7a), and a very strong 12-hour zonal wind perturbation on day 248 (Figure 7b). These were clearly long-period perturbations. To further investigate these perturbations, we examine lidar wind and temperature measurements over a long observation period at the altitudes where the ripples were observed. Shown in Figures 8a and 8b are the time series of hourly mean temperature and zonal and meridional winds at 87.5 and 88.5 km, respectively, for 3 September and 5 September. Since each data set is about 16 hours long (less than 24 hours), we fit the time series to a constant, plus 12-hour and 8-hour tidal periods. From best fits shown in Figure 8a, the 12-hour and 8-hour amplitudes for temperature and zonal and meridional winds for 3 September at 87.5 km were determined to be (15.6 ± 4.4 K, 51.1 ± 5.9 m/s, 33.7 ± 4.3 m/s) and (16.3 ± 4.3 K, 27.3 ± 5.5 m/s, 18.7 ± 3.9 m/s), respectively. From best fits shown in Figure 8b, the corresponding amplitudes at 88.5 km for 5 September were (4.3 ± 3.0 K, 64.8 ± 5.6 m/s, 79.6 ± 2.8 m/s) and (10.2 ± 2.7 K, 28.2 ± 5.5 m/s, 15.6 ± 2.7 m/s). There exists a large temperature maximum of ~30 K near 0600 UT in Figure 8a, resulting from the constructive interference between 12-hour and 8-hour period perturbations. On the other hand, the 12-hour perturbations in horizontal winds clearly dominate in Figure 8b; at ~0630 UT, the zonal and meridional wind shears were both large enough to possibly induce a dynamical instability.

[25] A recent study of atmospheric instability by *Liu et al.* [2004] analyzed 4 nights of wind and temperature observations from Starfire Optical Range (35°N), with 6–7 hours of data each night. The authors deduced that the low convective stability observed was mainly associated with the diurnal tide. With the data gaps existed during daytime, they were able to "resolve" both diurnal and semidiurnal tides only by constraining the analysis with the use of a

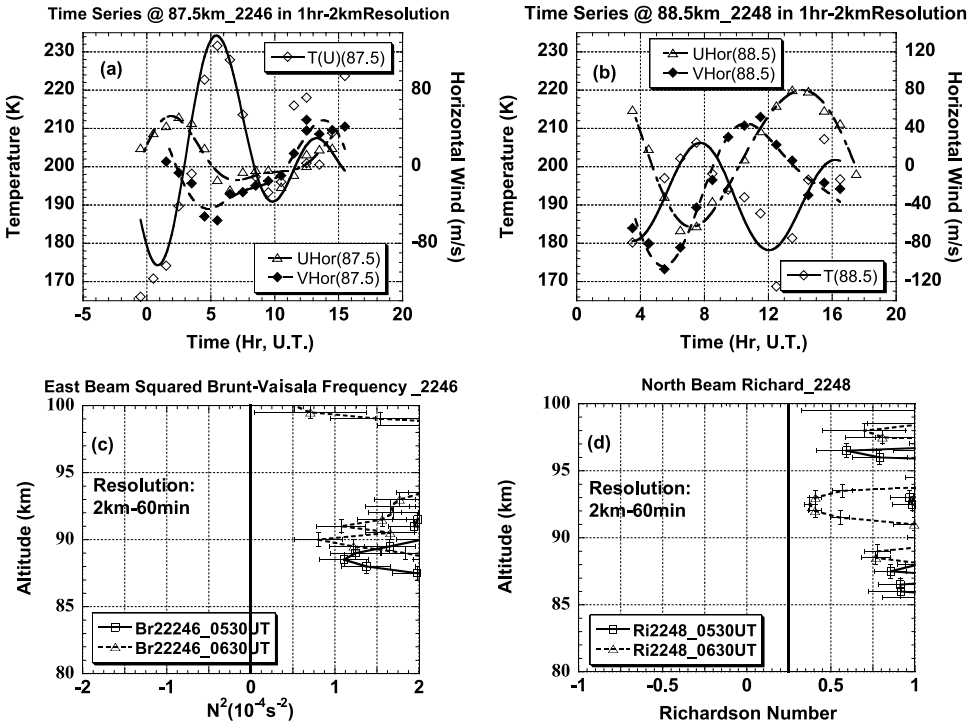


**Figure 8.** (a) Time series of hourly mean east beam temperature and zonal and meridional wind at 87.5 km on 3 September (day 2246) and (b) of hourly mean north beam temperature and zonal and meridional wind at 88.5 km on 5 September (day 2248). (c and d) Hourly mean profiles of east beam Brunt-Vaisala frequency squared on 3 September and of north beam Richardson number on 5 September, respectively, for 2 hours centered at 0530 and 0630 UT.

much-simplified model (single wavelength and single scale height for each tidal component) and of the mean values derived from a numerical model. While justifications for this analysis approach of the Starfire data were provided by the authors, because of the existence of considerable day-to-day variability in both the mean state and tide [*She et al.*, 2004a] and because alternative model assumptions would lead to different results, the reliability of their deduced results, in our view, may be questioned.

[26] Despite the high statistical quality of the fits shown in Figures 8a and 8b (i.e., R values ranging from 0.85 to 0.99), without a diurnal term, we were unable to resolve the relative importance between diurnal and semidiurnal tides with the current data. Fortunately, the problem of interest does not require such a resolution, for what we want to know is whether the long-period perturbations alone are sufficient to cause instability. For this purpose, we show two hourly mean profiles of $N^2$ and Ri between 0500 and 0700 UT with 2 km resolution, centered at each half hour for 3 September and 5 September, in Figures 8c and 8d, respectively. Since the convective billows occurred around 87.5 km on 0607:30 UT, 3 September, and the KH billows occurred around 88.5 km on 0622:30 UT, 5 September, we take note that the lowest values of $N^2$ at 87.5 km and of Ri at 88.5 km between the two hourly profiles are $\sim 1.0 \times 10^{-4}$ $s^{-2}$ (Figure 8c) and 0.75 (Figure 8d), respectively. Though these values are close to those required, the long-period perturbations alone are not low enough to cause respective instabilities. With the inclusion of shorter-period perturbations (i.e., the 1 and 1 km averages shown in Figures 3c and 6d) convective and dynamic instabilities are detected at the same altitudes where convective and KH billows were observed.

## 5. Discussion

[27] With the aid of concurrent lidar observations of temperature and horizontal wind, we have successfully characterized the nature of the observed ripples. By noting the nominal peak height of the OH layer being 87 ± 4 km [*She and Lowe*, 1998] and the computed vertical profiles of $N^2$ and Ri at the times when ripples were observed, we have not only determined the altitudes of the instability signatures to be 87.5 km and 88.5 km, but also the types of instabilities that are associated with each ripples. The peak height of OH layers observed by the SABER instrument [*Russell et al.*, 1999] during an overpass of the TIMED satellite was fortuitously centered at 87.5 km on 3 September and at 88.5 km on 5 September, respectively.

[28] By analyzing a longer data set of ~16 hours continuous observation, we have identified the relevant tidal period perturbations, showing that the mean state and tidal period perturbations (or simply long-period perturbations) alone are unable to cause the required instability for the generation of ripples, for which a superposed short-period wave or perturbation is required. This is so, despite the fact that the semidiurnal and terdiurnal tidal amplitudes in temperature for 3 September and those in zonal and meridional winds for 5 September were considerably larger than normal. Admittedly, because of undefined mean state/

diurnal period "interference" resulting from data gap, even with 16 hours continuous data, we still need to perform least squares harmonic fitting without the diurnal term. Unless the diurnal tidal amplitudes were reasonably small in September at a midlatitude location, the best fit values for the 12-hour and 8-hour components would be problematic.

[29] Fortunately, we recently have acquired a 9-day continuous day-night lidar observation in September 2003 and analyzed the tidal perturbations and variability from it. Contrary to the predictions of models like Global Scale Wave Model (GSWM00 and GSWM02) [*Hagan and Forbes*, 2003], the observation showed that the semidiurnal amplitudes for temperature and zonal and meridional winds at 86 km and 96 km were larger than the corresponding diurnal amplitudes by a factor between 1.5 and 10 [*She et al.*, 2004a], suggesting the dominance of semidiurnal tides in September over Fort Collins, Colorado (41°N). According to the classical tidal theory, the semidiurnal tides dominate at midlatitudes and high latitudes, though modern models, like GSWM consistently underestimate the semidiurnal tidal amplitudes. Radar wind measurements from globally distributed stations for a summer campaign in 1999 [*Pancheva et al.*, 2002] and from nearby Platteville, Colorado, with 2 years of observation [*Manson et al.*, 2003] also found agreement with GSWM00 prediction in diurnal tide and discrepancy in semidiurnal tides.

[30] At ~88 km, where ripples were observed, this 9-day continuous observation yields amplitudes of (5.5 K, 13.5 m/s, 6.5 m/s), (11.0 K, 28.5 m/s, 27.5 m/s), and (1.2 K, 6.2 m/s, 1.6 m/s), respectively, for diurnal, semidiurnal, and terdiurnal amplitudes of oscillations in (temperature, zonal wind, and meridional wind), the diurnal amplitudes are smaller than semidiurnal amplitudes by a factor of 2 or more. Unlike observations with data gaps, the results of the harmonic decomposition from the 9-day continuous data set are robust. We have fitted the time series of the 9-day continuous data to a constant plus (1) 4 harmonic terms with 24-, 12-, 8-, and 6-hour periods, (2) 2 terms with 24- and 12-hour period, and (3) 2 terms with 12- and 8-hour periods. The harmonic results from the fits to the 3 different scenarios are same. Furthermore, the semidiurnal and terdiurnal amplitudes deduced from this long data set are much smaller than the corresponding amplitudes of (16.6 K, 16.3 K) for temperatures on 3 September, and (64.8 m/s, 79.6 m/s) and (28.2 m/s, 15.6 m/s) for zonal and meridional winds on 5 September. All these suggest that we could conclude that (1) the unusually large temperature perturbation at ~0600 UT, 3 September, resulting from the constructive interference between 12-hour and 8-hour oscillations provided credible temperature gradient, and (2) the unusually large 12-hour period horizontal wind oscillation at ~0630 UT, 5 September, provided credible wind gradients, leading to a low atmospheric stability at the altitude and time of ripples. Superposition of these long-period waves with a short-period AGW with nominal amplitude is sufficient to nudge the atmosphere into local instability. Thus, following *Liu et al.* [2004], we have provided examples that showed unusually large tidal period oscillation can have strong influence on local instability. We also confirmed the general idea that tidal (or long-period) perturbations alone are typically not enough to cause local ility without a superimposed push from a short-period wave. However, the extent of the assessed instability depends on resolution of lidar measurements, a precise statement may be difficult. To muddy the water a bit more, we quote from *Fritts and Alexander* [2003, paragraph 130] that analysis showed that "local instability can occur at wave amplitudes below that often considered necessary for convective instability in many instances [*McEwan*, 1971; *Sonmor and Klaassen*, 1997]."

[31] With the nighttime (from 0200 to 1200 UT) temperature and zonal and meridional wind profiles at 1 km and 15 min resolution, we can compute the altitude-time distributions of convective instability ($N^2 < 0$) and dynamic instability ($0 < Ri < 0.25$) for both beams and both nights. The result of this computation is shown in Figure 9 with blue for east beam and red for north beam with convective instability and dynamic instability for 3 September shown in Figures 9a and 9b, respectively, and with those for 5 September shown in Figures 9c and 9d, respectively. The resolution of each instability cell is a rectangle with 1-km height and 15-min width. As expected, we see a blue cell centered at 87.5 km and 0607:30 UT in Figure 9a and a red cell at 88.5 km and 0622:30 UT in Figure 9d, corresponding to the occurrences of convective instability in the east beam, and of dynamic instability in the north beam that generated ripples were observed. At the same times and altitudes, we see neither red cell in Figure 9a nor blue cell in Figure 9d, suggesting that the instability structure is indeed localized. For the instability distribution plots (Figure 9) we restrict the investigation to a maximum temperature error of 5 K (with the corresponding wind error nominally of $\leq$15 m/s); a solid line labeled "5" marked this boundary of acceptable $N^2$ and Ri (Figure 9). The atmosphere was considerable difference between the nights of 2–3 and 4–5 September. Comparing Figure 9a to 9c, we note that the atmosphere was convectively less stable on the night of 2–3 September. On the night of 2–3 September, the occurrence frequency for convective (12.3% for east beam and 13.1% for north beam) and dynamic (14.9% and 13.8%) instabilities were comparable in the mesopause region, while on the night of 4–5 September, the atmosphere was much more likely to have become dynamically unstable with the occurrence frequencies for convective instability of 5.9% and 5.0% for east and north beams, and for dynamic instability of 18.2% and 16.2% correspondingly. We also noticed the very clear downward phase progressions of both convective and dynamic instability cells on the night of 2–3 September (not so for the night of 4–5 September), reflecting the presence of stronger wave activities that night. Between 84 and 91 km, observable by OH imager, we saw considerably more dynamically unstable cells between 0700 and 1100 UT on the night of 4–5 September, reflecting perhaps the nature of ripple patches observed in the image between 0800 and 0830, and later between 1020 and 1100 UT. In general, we saw many more regions of convective and dynamic instabilities between 84 and 91 km, but we observed only one ripple for each night that moved across either laser beam. Thus we have shown that ripple structures are indeed signatures of instability, but it appears that many unstable regions were observed without ripples in the OH image. This is quite analogous to our recent observation of temperature inver-

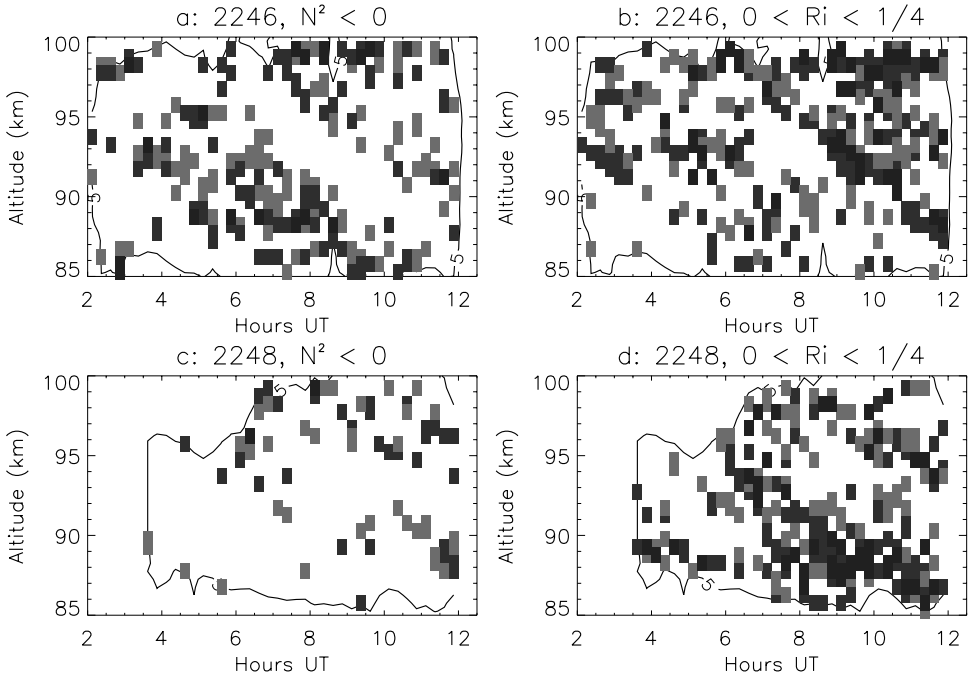


**Figure 9.** Regions with a superadiabatic lapse rate and possible convective instability for 3 September (Figure 9a) and 5 September (Figure 9c). The corresponding regions with a Richardson number between 0 and 1/4 are shown in Figures 9b and 9d. Blue indicates instability in the east beam, red indicates instability in the north beam, and purple indicates both in all four plots. A solid line encircles the region with temperature errors less than 5 K (and nominal wind errors less than 15 m/s). See color version of this figure at back of this issue.

sion accompanying a mesospheric bore [*She et al.*, 2004b], but we do not see mesospheric bores during every strong temperature inversion.

## 6. Conclusions

[32] We report the observation of two short-lived, wave-like features, known as ripples, by the OH imager located at Platteville, Colorado, between 0600 and 0630 UT on 3 September and 5 September 2002, respectively. From the successive images, we determined the wavelength of the ripples to be ~9 km and ~7 km, and their lifetime to be ~9 min and ~15 min, as well as the speed and direction of the motion of these ripple patterns. The phase fronts of both ripples were found to be approximately perpendicular to the phase fronts of a nearby propagating AGW.

[33] With the help of concurrent lidar observations of temperature and zonal and meridional winds, we were able to determine the nature of the ripples observed in the OH all-sky imager. We found the 3 September ripple located at 87.5 km to be induced by a convective instability, and the 5 September ripple at 88.5 km, by a dynamic instability. Hodographs of lidar measured wind shear vectors revealed that a speed shear was associated with the observed convective billows, whose phase fronts was approximately parallel to the wind shear, and that a directional shear was associated with the observed KH billows, whose phase fronts was approximately perpendicular to the wind shear. Unlike that reported by *Yamada et al.* [2001], we note that since the wind shear happens to be parallel to the ripples' phase fronts in the case of the convective billows, there was no rotation after its for , and its phase fronts remain perpendicular to the phase fronts of the associated AGW, in agreement with the alignment predicted by simulation. This conceptual understanding as reviewed by *Hecht* [2004] also allowed us to compare the nature of both convective and dynamic billows we observed to those ripples in the earlier observations, as tabulated in Table 1. The ratios of ripple's wavelength to the depth of the unstable regions were also examined. Since the extent of instability depends on the resolution of lidar measurements, and the exact theoretical definition for the depth of an instability region was not sharp, it is difficult to draw a firm conclusion. Within stated error bars, our observations of this ratio for both convective and dynamic cases are in general agreement with previous observations [*Larsen*, 2000; *Hecht*, 2004], which were in agreement with theory for dynamically induced ripples, and a factor of ~2 larger than the prediction of simulation for the convective case.

[34] We have also computed the values of $N^2$ and Ri using both hourly mean and 15-min mean lidar temperature and horizontal wind profiles. For the convective billows, we found $N^2 = 1.0 \times 10^{-4}$ $s^{-2}$ from the hourly mean temperature profile, and $N^2 < 0$ from the 15-min profile. For the KH billows, we found Ri = 0.75 and Ri < 0.25 for the 1-hour and 15-min cases, respectively. This comparison suggests that long-period perturbations alone are not sufficient to reduce atmospheric stability to that required for generation of ripples in both cases. Superposition with a short-period AGW appears to do the trick, yielding local atmospheric instability for ripple generation. Using the data from 16 hours continuous observation in each case, we have made a tidal decomposition of hourly mean temperature and zonal and meridional winds into the sum of constant,

12-hour and 8-hour terms at the ripples' altitudes. Compared to the tidal amplitudes resulting from the 9-day continuous data set, the temperature perturbation existed on 3 September, resulting from the constructive interference between 12-hour and 8-hour perturbations, and the 12-hour zonal and meridional wind perturbations existed on 5 September were unusually large. These unusually large tidal components were likely responsible for the long-period oscillations that prepared the background atmosphere to be in near instability.

[35] In summary, we have presented two observations of ripple structure by OH imager. The concurrent measurements of mesopause region temperature and zonal and meridional wind allowed us to characterize the nature of these instability patterns and deduce that one ripple was induced by convective instability and the other was induced by dynamic instability. Lidar data sets provided us means not only to compare with previous reported observations but also to validate theoretical predictions quantitatively. With more concurrent lidar-imager observation of ripples, one may be able to investigate more fully the causal relations between ripples and atmospheric instabilities, as well as to deduce atmospheric conditions under which the instability could lead to wave breaking. As imagers and lidars become more available, this type of study bounds to increase. One more case of instability-induced ripple was recently reported [*Hecht et al.*, 2005] after the submission of this article, tipping the balance of Table 1 in favor of dynamic instability.

[36] **Acknowledgments.** We express our heartfelt thanks to David C. Fritts for many pedagogical discussions on the subject of gravity waves both during the preparation of this study and over past years. C. Y. She thanks Jim Hecht for answering questions and providing references on ripples. This work is supported in part by grants from the National Aeronautics and Space Administration, NAG5-10076 and NAG5-13567, and from the National Science Foundation, ATM-0003171, ATM-0335127, and ATM-0137555.

## References

Andreassen, Ø., C. E. Wasberg, D. C. Fritts, and J. R. Isler (1994), Gravity wave breaking in two and three dimensions: 1. Model description and comparison of two-dimensional evolutions, *J. Geophys. Res.*, *99*, 8095–8108.

Broadfoot, A. L., and K. R. Kendall (1968), The airglow spectrum, 3100–10000A, *J. Geophys. Res.*, *73*, 426–428.

Chen, H., M. A. White, D. A. Krueger, and C. Y. She (1996), Daytime mesopause temperature measurements using a sodium-vapor dispersive Faraday filter in lidar receiver, *Opt. Lett.*, *21*, 1003–1005.

Cutler, L. J., R. L. Collins, K. Mizutani, and T. Itabe (2001), Rayleigh lidar observations of mesospheric inversion layers at Poker Flat, Alaska 67°N, 147°W, *Geophys. Res. Lett.*, *28*, 1467–1470.

Dutton, J. A. (1986), *The Ceaseless Wind: An Introduction to the Theory of Atmospheric Motion*, chap. 4, pp. 75–79, Dover, Mineola, N. Y.

Franke, P. M., and R. L. Collins (2003), Evidence of gravity wave breaking in lidar data from the mesopause region, *Geophys. Res. Lett.*, *30*(4), 1155, doi:10.1029/2001GL014477.

Fritts, D. C., and M. J. Alexander (2003), Gravity wave dynamics and effects in the middle atmosphere, *Rev. Geophys.*, *41*(1), 1003, doi:10.1029/2001RG000106.

Fritts, D. C., and P. K. Rastogi (1985), Convective and dynamical instabilities due to gravity wave motions in the lower and middle atmosphere: Theory and observations, *Radio Sci.*, *20*(6), 1247–1277.

Fritts, D. C., J. R. Isler, and Ø. Andreassen (1994), Gravity wave breaking in two and three dimensions: 2. Three dimensional evolution and instability structure, *J. Geophys. Res.*, *99*, 8109–8123.

Fritts, D. C., J. F. Garten, and Ø Andreassen (1996), Wave breaking and transition to turbulence in stratified shear flows, *J. Atmos. Sci.*, *53*, 1057–1085.

Fritts, D. C., J. R. Isler, J. H. Hecht, R. L. Walterscheid, and Ø. Andreassen (1997), Wave breaking signatures in OH airglow and sodium densities and temperatures: 2. Simulation of wave and instability structures, *J. Geophys. Res.*, *102*, 6669–6684.

Hagan, M. E., and J. M. Forbes (2003), Migrating and nonmigrating semidiurnal tides in the upper atmosphere excited by tropospheric latent heat release, *J. Geophys. Res.*, *108*(A2), 1062, doi:10.1029/2002JA009466.

Hecht, J. H. (2004), Instability layers and airglow imaging, *Rev. Geophys.*, *42*, RG1001, doi:10.1029/2003RG000131.

Hecht, J. H., R. L. Walterscheid, D. C. Fritts, J. R. Isler, D. C. Senft, C. S. Gardner, and S. J. Franke (1997), Wave breaking signatures in OH airglow and sodium denstities and temperatures. 1: Airglow imaging, Na lidar, and MF radar observations, *J. Geophys. Res.*, *102*, 6655–6668.

Hecht, J. H., C. Fricke-Bergemann, R. L. Walterscheid, and J. Hofner (2000), Observations of the breakdown of an atmospheric gravity wave near the cold summer mesopause at 54N, *Geophys. Res. Lett.*, *27*, 879–882.

Hecht, J. H., R. W. Walterscheid, and R. A. Vincent (2001), Airglow observations of dynamical (wind shear-induced) instabilities over Adelaide, Australia, associated with atmospheric gravity waves, *J. Geophys. Res.*, *106*, 28,189–28,197.

Hecht, J. H., A. Z. Liu, R. L. Walterscheid, and R. J. Rudy (2005), Maui Mesosphere and Lower Thermosphere (Maui MALT) observations of the evolution of Kelvin-Helmholtz billows formed near 86 km altitude, *J. Geophys. Res.*, *110*, D09S10, doi:10.1029/2003JD003908.

Hines, C. O. (1960), Internal gravity waves at ionospheric heights, *Can. J. Phys.*, *38*, 1441–1481.

Holton, J. R. (1982), The role of gravity wave induced drag and diffusion in the momentum budget of the mesosphere, *J. Atmos Sci.*, *39*, 791–799.

Houghton, J. T. (1978), The stratosphere and mesosphere, *Q. J. R. Meteorol. Soc.*, *104*, 1–29.

Isler, J. R., D. C. Fritts, Ø. Andreassen, and C. E. Wasberg (1994), Gravity wave breaking in two and three dimensions: 3. Vortex breakdown and transition to isotropy, *J. Geophys. Res.*, *99*, 8125–8138.

Larsen, M. F. (2000), A shear instability seeding mechanism for quasi-periodic radar echos, *J. Geophys. Res.*, *105*, 24,931–24,940.

Li, F., A. Z. Liu, G. R. Swenson, J. H. Hecht, and W. A. Robinson (2005), Observations of gravity wave breakdown into ripples associated with dynamical instabilities, *J. Geophys. Res.*, *110*, D09S11, doi:10.1029/2004JD004849.

Liu, A. Z., R. G. Roble, J. H. Hecht, M. F. Lasen, and C. S. Gardner (2004), Unstable layers in the mesopause region observed with Na lidar during the Turbulent Oxygen Mixing Experiment (TOMEX) campaign, *J. Geophys. Res.*, *109*, D02S02, doi:10.1029/2002JD003056.

Lloyd, K. H., C. H. Low, and R. A. Vincent (1973), Turbelence, billows, and gravity waves in high shear region of the upper atmosphere, *Planet. Space Sci.*, *21*, 653–661.

Manson, A. H., C. E. Meek, S. K. Avery, and D. Thorsen (2003), Ionospheric and dynamical characteristics of the mesosphere-lower thermosphere region over Platteville (40°N, 105°W) and comparisons with the region over Saskatoon (52°N, 107°W), *J. Geophys. Res.*, *108*(D13), 4398, doi:10.1029/2002JD002835.

McEwan, A. D. (1971), Degeneration of resonantly excited standing internal gravity waves, *J. Fluid Mech.*, *50*, 431–448.

Nakamura, T., A. Higashikawa, T. Tsuda, and Y. Matsushita (1999), Seasonal variations of gravity wave structures in OH airglow with a CCD imager at Shigaraki, *Earth Planets Space*, *51*, 897–906.

Pancheva, D., et al. (2002), Global-scale tidal structure in the mesosphere and lower thermosphere during PSMOS campaign of June–August 1999 and comparison with the global-scale wave model, *J. Atmos. Sol. Terr. Phys.*, *64*, 1011–1035.

Peterson, A. W. (1979), Airglow events visible to the naked eye, *Appl. Opt.*, *22*, 3390–3393.

Peterson, A. W., and L. M. Kieffaber (1973), Infrared photography of OH airglow structures, *Nature*, *242*, 321–322.

Russell, J. M., III, et al. (1999), An overview of the SABER experiment and preliminary calibration results, *Proc. SPIE Int. Soc. Opt. Eng.*, *3756*, 277–288.

She, C. Y., and R. P. Lowe (1998), Seasonal temperature variations in the mesopause region at mid-latitude: Comparison of lidar and hydroxyl rotational temperatures using WINDII/UARD OH height profiles, *J. Atmos. Sol. Terr. Phys.*, *60*, 1573–1583.

She, C. Y., et al. (2004a), Tidal perturbations and variability in mesopause region over Fort Collins, CO (41N, 105W): Continuous multi-day temperature and wind lidar observations, *Geophys. Res. Lett.*, *31*, L24111, doi:10.1029/2004GL021165.

She, C. Y., T. Li, B. P. Williams, T. Yuan, and R. H. Picard (2004b), Concurrent OH imager and sodium temperature/wind lidar observation of a mesopause region undular bore event over Fort Collins/Platteville, CO, *J. Geophys. Res.*, *109*, D22107, doi:10.1029/2004JD004742.

Sherman, J., B. P. Williams, T. D. Kawahara, D. A. Krueger, and C. Y. She (2003), A dynamical study of the winter mid-latitude mesopause region (80–105 km) based on initial simultaneous lidar measurements of temperature, and winds over Fort Collins, CO (41N, 105W), *Adv. Space Res.*, *32*, 753–758.

Shiokawa, K., Y. Katoh, M. Sayoh, M. K. Ejjri, T. Ogawa, T. Nakamura, T. Tsuda, and R. H. Weins (1999), Development of Optical Mesosphere Thermosphere Imagers (OMTI), *Earth Planets Space*, *51*, 887–896.

Sica, R. J., and M. D. Thorsley (1996), Measurements of superadiabatic lapse rates in the middle atmosphere, *Geophys. Res. Lett.*, *23*, 2797–2800.

Sonmor, L. J., and G. P. Klaassen (1997), Toward a unified theory of gravity wave stability, *J. Atmos. Sol. Terr. Phys.*, *54*, 2655–2680.

Swenson, G. R., and S. B. Mende (1994), OH emission and gravity waves (including breaking wave) in all-sky imagery from Bear Lake, UT, *Geophys. Res. Lett.*, *21*, 2239–2242.

Taylor, M. J., and M. A. Hapgood (1990), On the origin of ripple-type structure in the OH nightglow emission, *Planet. Space Sci.*, *38*, 1421–1430.

Taylor, M. J., D. C. Fritts, and J. R. Isler (1995), Determination of horizontal and vertical structure of an unusual pattern of short period gravity waves imaged during ALOHA-93, *Geophys. Res. Lett.*, *22*, 2837–2840.

Taylor, M. J., W. R. Pendleton Jr., S. Clark, H. Takahashi, D. Gobbi, and R. A. Goldberg (1997), Image measurements of short-period gravity waves at equatorial latitudes, *J. Geophys. Res.*, *102*, 26,283–26,299.

Williams, B. P., M. A. White, D. A. Krueger, and C. Y. She (2002), Observation of a large amplitude wave and inversion layer leading to convective instability in the mesopause region over Fort Collins, CO (41°N, 105°W), *Geophys. Res. Lett.*, *29*(17), 1850, doi:10.1029/2001GL014514.

Yamada, Y., H. Fukunishi, T. Nakamura, and T. Tsuda (2001), Breaking of small-scale gravity waves and transition to turbulence observed in OH image, *Geophys. Res. Lett.*, *28*, 2153–2156.

Zhao, Y., A. Z. Liu, and C. S. Gardner (2003), Measurements of atmospheric stability in the mesospause at Starfire optical range, NM, *J. Atmos. Sol. Terr. Phys.*, *65*, 219–232.

R. L. Collins, Geophysical Institute, University of Alaska Fairbanks, Fairbanks, AK 99775, USA.

L. M. Kieffaber and A. W. Peterson, Department of Physics, Whitworth College, Spokane, WA 99251, USA.

T. Li, C. Y. She, B. P. Williams, and T. Yuan, Department of Physics, Colorado State University, Fort Collins, CO 80523, USA. (joeshe@lamar.colostate.edu)

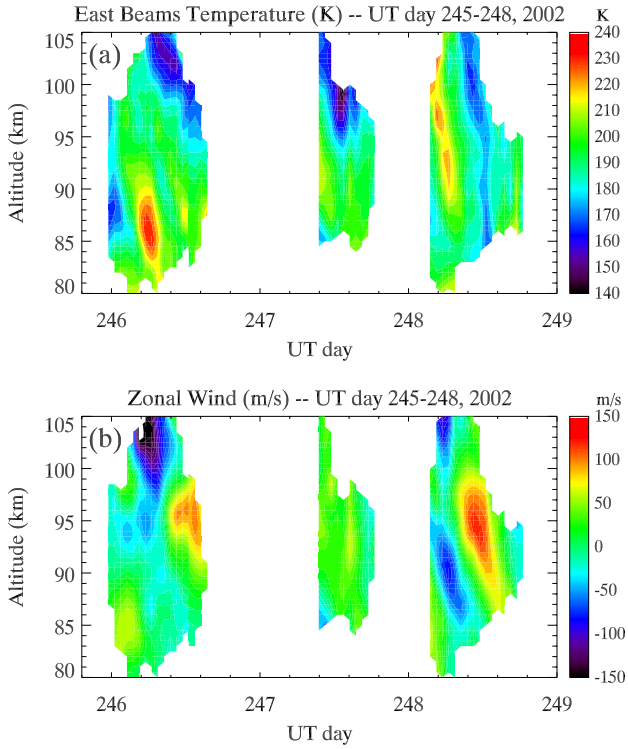


**Figure 7.** Altitude-time contour plots of (a) east beam temperatures and (b) zonal winds. The temperature data (Figure 7a) show a strong vertical temperature gradient between 85 and 90 km on 3 September. The zonal wind (Figure 7b) shows an unusually strong 12-hour perturbation between 85 and 95 km on 5 September. These are thought to be due to tidal period perturbations (see text).

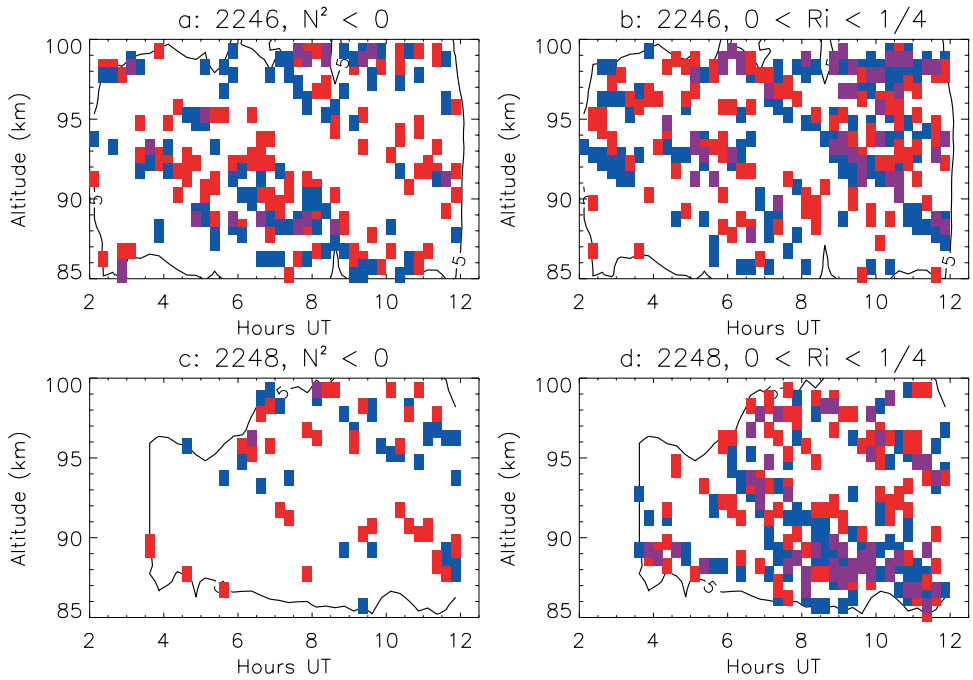


**Figure 9.** Regions with a superadiabatic lapse rate and possible convective instability for 3 September (Figure 9a) and 5 September (Figure 9c). The corresponding regions with a Richardson number between 0 and 1/4 are shown in Figures 9b and 9d. Blue indicates instability in the east beam, red indicates instability in the north beam, and purple indicates both in all four plots. A solid line encircles the region with temperat ors less than 5 K (and nominal wind errors less than 15 m/s).